Isotropic Grids Revisited: A Numerical Study of Solar Cell Electrode Geometries

Oliver Nakano-Baker, Clay Boyd, Caitlin Cramer, Lucien Brush, and J. Devin MacKenzie

***Abstract*— Many contemporary solar cells utilize sparse front electrodes to gather charge carriers from the sun-facing side of their active material layers, deploying an H-bar shape to minimize shadowing and resistive losses in the cell material and metal lines. Isotropic grids, comprised of overlapping line arrays and forming triangular, square, or hexagonal shapes, are generally not recognized as outperforming H-bar type designs as front electrodes due to their increased shadowing. However, for solar cells where front-side charge carriers converge to single point sinks, and especially when transparent conductor (TC) sheet resistance is high, isotropic grids are capable of outperforming H-bars. We present a simple numerical framework for modeling the shadow and resistive losses in circular H-bar and isotropic grids and for optimizing the pitch and width of the designs. Using Griddler finite element (FE) software as validation, we demonstrate that isotropic grids produce more power for solar cells with high transparent conductive layer resistance and point sinks.**

***Index Terms*— Contacts, design optimization, electrodes, modeling, photovoltaic cells.**

I. Introduction

FRONT electrode metallization of a solar cell performs the critical function of collecting charge carriers. Its intrinsic role is straightforward as a simple metallic conductor; however, it presents a characteristic design challenge: large metal lines that minimize resistive losses to overall power conversion efficiency cast a larger shadow on the underlying solar cell material, reducing harvestable photogenerated current. The optimization of these two characteristic losses has been well studied both numerically and experimentally [1]–[14].

Manuscript received March 7, 2022; revised April 30, 2022; accepted May 3, 2022. Date of publication May 27, 2022; date of current version June 21, 2022. This material is based in part upon work supported by the state of Washington through the Washington Research Foundation and the University of Washington Clean Energy Institute. The review of this article was arranged by Editor H. Nguyen. *(Corresponding author: Oliver Nakano-Baker.)*

Oliver Nakano-Baker is with the Department of Materials Science and Engineering, University of Washington, Seattle, WA 98195 USA (e-mail: onb@uw.edu).

Clay Boyd is with the Department of Electrical and Computer Engineering, University of Washington, Seattle, WA 98195 USA.

Caitlin Cramer was with the Department of Materials Science and Engineering, University of Washington, Seattle, WA 98195 USA.

Lucien Brush is with the Department of Materials Science and Engineering, the Department of Mechanical Engineering, and the Department of Applied Mathematics, University of Washington, Seattle, WA 98195 USA (e-mail: brush@uw.edu).

J. Devin MacKenzie is with the Department of Materials Science and Engineering and the Department of Mechanical Engineering, University of Washington, Seattle, WA 98195 USA (e-mail: jdmacken@uw.edu).

Color versions of one or more figures in this article are available at https://doi.org/10.1109/TED.2022.3174810.

Digital Object Identifier 10.1109/TED.2022.3174810

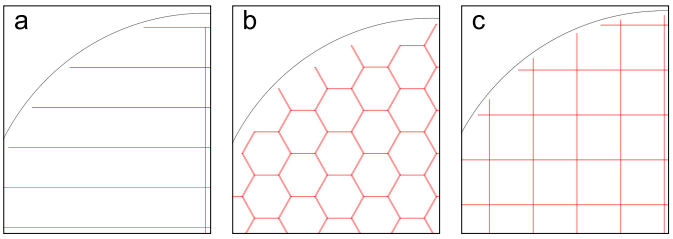

Fig. 1. Optimized layouts of 5-cm-diameter circular front cell electrode designs using (a) H-bar, (b) hexagonal, and (c) square grid layouts.

In general, the principal power losses created by a solar cell's front electrode array arise from the array's shadow, resistive losses in the lines, and resistive losses in the underlying front semitransparent conductive sheet or heavily doped semiconductor as current transports laterally from near the sites of photogeneration in cell active layers to the grid.

Most grid designs utilize parallel lines that intersect a perpendicular bus bar, referred to here as an "H-bar" design. A second class of isotropic grids includes all regular tessellating planar unit cells: closed hexagons, triangles, or squares. Examples of H-bar, hexagon, and square patterns are shown in Fig. 1.

The isotropic grids have long been understood to have inferior properties to H-bar grids for a basic front electrode array application [1]. At equivalent pitch with all other materials and dimension held equal, isotropic grids incur a $2\times$ increase in shadowing losses while enjoying no benefit to their current transport efficiency compared to H-bar patterns. For this reason, virtually, all contemporary solar cell modules utilize front H-bar electrodes of some flavor [15].

A. Revisiting Isotropic Grids

Two features of emerging solar cell design motivate a reexamination of the isotropic family of grid designs: the shift to point sinks in modern cell layouts and the competitiveness of high-resistance front layers in thin-film solar cells. The first of these comes from the use of through-stack vias by many commercial modules; vias shuttle current to a rear-side bus and are point sinks for the front-side charge carriers [16]. In these architectures, H-bar electrodes result in an indirect current pathway to the sink where isotropic grids would perform transport along an effectively straight pathway and with the same efficiency of transport as the H-bar.

The second feature is the competitiveness of high transparent conductor (TC) resistance (ρ_{TC}) solar cell module designs. TCs constitute layers of a device that confer an ability to

transport current in the plane of the device while being mostly transparent to light, excluding front metallization. Thin-film photovoltaic modules, such as perovskites, cadmium telluride, and organic photovoltaics, commonly use dedicated TC layers such as indium tin oxide (ITO) on their front face to effect charge carrier transport from the active material to the edge of the cell or an electrode grid. ITO layers are expensive and give rise to unavoidable optical extinction losses due to the inherent tradeoffs between metallic-like conductivity derived from their significant carrier concentrations and absorption and reflectivity. Sourcing materials for their manufacture can be geopolitically challenging, leading to much research into their replacement [17], [18], i.e., by conductive polymers or nanowire layers.

For many such layers, Jacobs *et al.* [19] contended that it is advantageous to increase the sheet resistivity of the TC and thus minimize optical extinction beyond the traditional ~10 Ω/sq, with values up to 10-kΩ/sq optimal for some systems. In addition, the high charge carrier mobility of perovskite photovoltaics could motivate the deployment of TC-free, high-resistance, low-extinction modules [20], [21]. Isotropic grids with fine pitch should excel in these high-ρ_{TC} design spaces due to lower diffusion distances, aiding in the minimization or elimination of ITO layers.

New additive manufacturing pathways for metal lines are being explored [22]–[24] and there is interest in thin-film tandem architectures, which can require multiple TC layers within a solar cell stack [25]. These developments perturb the established material properties and design assumptions in commercial solar cell modules. With solar panels providing an ever-increasing share of worldwide utility-scale power, incremental improvements in efficiency and output can result in significant power gains and competitiveness. For example, a mere 1% relative increase in module efficiency would have corresponded to an additional 3.65 TWh of solar energy produced in USA in 2020, worth about $389 million at the going utility rate [26]. Considering solar's growing market and shifting design landscape, it is an ideal time to reexamine old assumptions around front contact design, including the supremacy of the H-bar layout.

B. Solar Cell Grid Optimization

Strategies for the optimization of solar cell grids have evolved significantly over the past 50 years. Early studies by Napoli *et al.* [1] and Serreze [2] established numerical models for the individual sources of power loss in straight- and tapered-line grids, respectively. Such models are suited to rapid numerical optimization, and this study employs similar methods to revisit isotropic transport grids. We assume the simplest possible conditions, including single values for linewidth and pitch and constant wire height. However, alternate design approaches exist, which improve grid performance at the cost of increased complexity and expanded design space.

Most importantly, it is optimal to vary grid linewidths locally according to the relationships outlined by Scharlack [3], with every wire scaled to an optimal width relative to solar current, local wire current, and material constants. The relationship has been utilized by later works, including spoked radial grids for circular cells [7], [9]. The losses in such a system mirror basic scaling laws found in biological systems [27], [28] and the basic tenet can be stated that the optimal size of transport elements in a network will scale so as to maintain a constant optimal flux density everywhere in the network.

More recently, grid optimization is often expanded to include module-scale bus bar and material cost optimization [12], [14]. Some grid design strategies abandon the notion of fixed-pitch grids, adopting free-form approaches. These strategies range from strategic addition or subtraction of grid elements [11] to free-form design of ramified transport networks [8], [29] and can potentially be adopted to arbitrary solar module geometries [30]. We expect these networks to outperform both the H-bar and isotropic designs presented here by benefiting from more direct current pathways without the high shadowing cost of the isotropic grids; however, this comes at the cost of a significantly more complex optimization landscape.

In this study, we rederive basic numerical equations for the principal losses in a front electrode isotropic grid pattern and verify the model using the commercially available Griddler simulation package [31]. The numerical models are used to design optimal H-bar and isotropic grids for high-ρ_{sheet} point-sink solar cells, and their relative performance is evaluated using Griddler's finite element (FE) solar cell simulator. Areas of point-sink solar cell design space are identified where an isotropic grid pattern outperforms H-bar grids.

TABLE I
SYMBOLS AND UNITS FOR FRONT GRID NUMERICAL MODELS

Symbol	Description	Units
R	Solar cell radius	cm
b	Grid pitch	cm
w	Grid wire width	cm
h	Grid wire height	cm
ϵ	Sink radius	cm
ρ_{metal}	Metallization resistivity	$\Omega\ cm$
ρ_{TC}	Transparent conductor sheet resistance	Ω/sq
J_{sol}	Solar current density	A/cm^2
V_{op}	Operating voltage	V

II. METHODS

To compare H-bar and isotropic patterns, numerical models were used to estimate the main sources of power loss in the front metallization: shadowing, grid line resistance, and TC resistance. Symbols and units for these calculations are defined in Table I and shown in Fig. 2.

Convex optimization of the numerical expressions was used to rapidly identify near-optimal configurations of H-bar and isotropic grids on circular solar cells with a single central current sink. Both grid types were optimized across a range of material properties and cell radii, and optimal designs were modeled using Griddler software to determine their peak power output. These FE-calculated power estimates were used to compare the performance H-bar and isotropic grids.

A notable omission from this study is the consideration of contact losses between TC and grid, as well as downstream

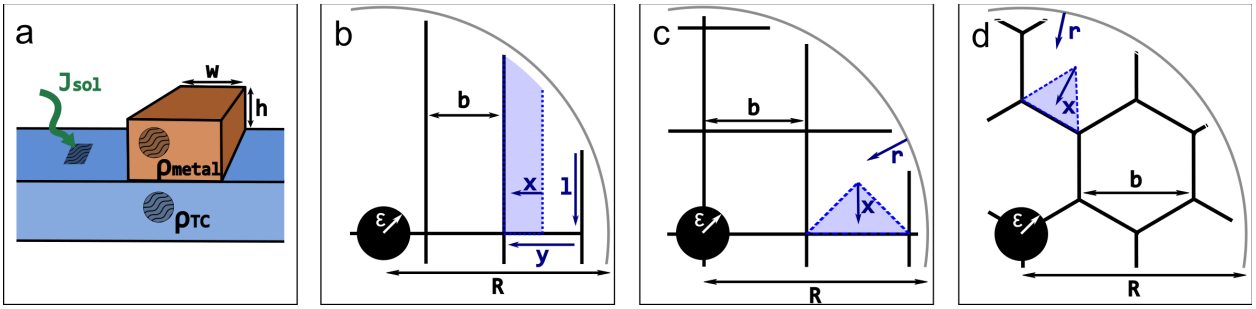

Fig. 2. Schematic layout of (a) grid cross section, (b) H-bar, (c) square, and (d) hexagonal grids. Unit tiles used for TC resistive loss calculations are demarked in dotted blue.

contact losses such as where lines intersect with bus bars. These power losses are typically smaller by an order of magnitude than the other power losses considered here and are a secondary source of loss for most practical solar cell modules [12].

A. Calculating Power Losses

We derive closed numerical equations for the shadow, line resistance, and TC sheet resistance losses in H-bar and isotropic grid arrangements on a circular solar cell. As standardized in former works [1], [3]–[6], grid resistive losses were calculated in watts as

$$P_{\text{lost}} = \int_j^k I(x)^2 \delta R(x) \tag{1}$$

where j and k are locations where current begins and ends, respectively; $I(x)$ is the cumulative current in amperes at location x, and $\delta R(x)$ represents an increment of resistance at location x. Generally, this can be expressed as

$$\delta R(x) = \frac{\rho}{l(x)} \delta x \tag{2}$$

where ρ is the sheet resistance (in ohm per square) of the transporting medium, $l(x)$ is the width of the transporting medium, and δx is an incremental distance along the direction of current flux. When transporting through an array of metal lines, the effective grid sheet resistances ρ of both H-bar and isotropic grids are

$$\rho_{\text{grid}} = \frac{\rho_{\text{metal}} b}{w h} \tag{3}$$

where ρ_{metal} is the metal resistivity, b is the pitch of the grid as shown in Fig. 2, and w and h are the width and height, respectively, of the metal lines. The effective grid sheet resistivity holds only in the direction parallel to the metal lines in an H-bar grid, but it is isotropic in the plane of the device for triangle, square, and hexagon grids. The equivalence and isotropic nature of these grids is demonstrated in the Appendix.

The maximum theoretical power gathered by a circular solar cell (i.e., with a lossless front grid) would be

$$P_{\text{max}} = J_{\text{sol}} V_{\text{op}} \pi R^2 \tag{4}$$

where J_{sol} is the solar current density, V_{op} is the cell operating voltage, and R is the radius of the circular cell. Shadow loss can be expressed as a fractional decrease in the max power due to the proportion of device stack area covered by metal lines. For H-bars, this is simply the ratio of width to pitch; for isotropic grids, the shadow loss is doubled. We have

$$P^{\text{Hbar}}_{\text{shadow loss}} = P_{\text{max}} \frac{w}{b} \tag{5}$$

$$P^{\text{iso}}_{\text{shadow loss}} = 2\, P_{\text{max}} \frac{w}{b}. \tag{6}$$

In the following, we outline simple models for the resistive losses in the two grid types on a circular cell.

1) Isotropic Grid Losses: The three non-H-bar grids all have isotropic conductivity in the solar cell plane and are equivalent to each other in terms of their grid resistive losses, see the Appendix for a demonstration of this effect. As long as the solar cell is large enough to contain many unit cells, i.e., $R \gg b$, current can effectively be assumed to travel radially from any point in the solar cell to the central sink. Cumulative current generated between the solar cell edge and radial position r is

$$I^{\text{iso}}_{\text{cumulative}}(r) = J_{\text{sol}} \pi (R^2 - r^2). \tag{7}$$

This expression can be combined with (3) for the grid effective sheet resistance into (1) and (2), taking the width $l(x) = 2\pi r$ because current at position r moves radially through a circumferential slice of material. The total power lost due to grid resistance is

$$P^{\text{iso}}_{\text{grid loss}} = \int_\epsilon^R I^{\text{iso}}_{\text{cumulative}}(r)^2 \frac{\rho_{\text{grid}}}{2\pi r} \delta r \tag{8}$$

where ϵ is the radius of the center point sink. The trend is resolved using numerical integration in the software model.

Resistive losses in the TC are generated as current diffuses across a triangular unit cell, as shown in Fig. 2. The variable x is defined to be the distance from the tip of this triangle on a path perpendicular to the nearest line, i.e., $x = b/2$ defines the coordinate where current reaches the conductive grid. It is assumed that current is evenly distributed to achieve uniform flux at every x, and we solve this equation for both square and hexagonal grids. The cumulative current in the TC can be written as

$$I^{\text{square}}_{\text{cumulative}}(x) = J_{\text{sol}} x^2 \quad I^{\text{hex}}_{\text{cumulative}}(x) = \frac{1}{\sqrt{3}} J_{\text{sol}} x^2. \tag{9}$$

Using (2) with $\rho = \rho_{TC}$, $l^{square}(x) = 2x$, and $l^{hex}(x) = (2/(3)^{1/2})x$, substitute into (1)

$$P_{TC\ loss}^{square\ unit\ cell} = \int_0^{\frac{b}{2}} J_{sol}^2 x^4 \frac{\rho_{TC}}{2x} \delta x = \frac{1}{128} J_{sol}^2 b^4 \rho_{TC} \quad (10)$$

and

$$P_{TC\ loss}^{hex\ unit\ cell} = \int_0^{\frac{b}{2}} \frac{1}{3} J_{sol}^2 x^4 \frac{\sqrt{3}\rho_{TC}}{2x} \delta x = \frac{\sqrt{3}}{384} J_{sol}^2 b^4 \rho_{TC}. \quad (11)$$

This accounts for loss in one unit cell. To estimate power loss across the entire solar cell, scale up using a ratio of areas, with $A = \pi R^2$, $A_{square} = (b^2/4)$, and $A_{hex} = (b^2/4(3)^{1/2})$

$$P_{TC\ loss}^{iso} = P_{TC\ loss}^{square\ unit\ cell} \frac{A}{A_{square}} = P_{TC\ loss}^{hex\ unit\ cell} \frac{A}{A_{hex}} = \frac{\pi}{32} J_{sol}^2 b^2 R^2 \rho_{TC}. \quad (12)$$

Power loss density is obtained by dividing the circular area A. This is not possible for grid losses, which depend on R. With identical models describing their shadow, grid-, and TC-resistive losses, the various isotropic grids are effectively interchangeable in this analysis.

2) H-Bar Grid Losses: Resistive losses in the H-bar grid are calculated in two parts. First, losses in a parallel array of lines with width w, height h, and pitch b are calculated, with current traveling from the area of the cell to a single cross-cell bus. Then, losses in the bus are calculated as current travels to the center sink. Using the sheet resistance description of the line array from (3), the loss in a strip of the line array intersecting and perpendicular to the bus, of length L and width δy, can be calculated. Recognizing that the current at distance l from the cell's edge will be $J\, l\, \delta y$, from (1), we have

$$P_{segment}(L) = \int_0^L (J_{sol}\, l\, \delta y)^2 \frac{\rho_{grid}}{\delta y} \delta l = \frac{1}{3} J_{sol}^2 L^3 \rho_{grid} \delta y. \quad (13)$$

The length of the array lines as one travels away from the central sink can be expressed as $L = f(y) = (R^2 - y^2)^{1/2}$, where y is the distance from the sink where the array intersects the bus line. (Note that as $y \to R$ at the end of the bus bar, the length of the array, and its associated resistive losses, go to zero.) The total resistive loss in the array comes from integrating this value numerically across all four quadrants of the cell

$$P_{grid\ loss}^{Hbar\ array} = 4 \int_0^R \frac{1}{3} J_{sol}^2 (R^2 - y^2)^{3/2} \rho_{grid}\, \delta y. \quad (14)$$

Resistive losses in the bus bar come from similarly integrating from the cell's edge to the sink the current incident from the array on the bus. The current in the bus at position y is

$$I_{bus}(y) = \int_y^R 2\ J_{sol} \sqrt{R^2 - y^2} \delta y \quad (15)$$

and the total power loss from both sides of the bus is solved using numerical integration in implementation as

$$P_{grid\ loss}^{Hbar\ bus} = 2 \int_\epsilon^R I_{bus}(y)^2 \rho_{grid}\, \delta y \quad (16)$$

where ϵ is the radius of the center point sink.

Device TC resistive losses for an H-bar grid are derived in past works [1], [3]. For this study, loss is calculated over the R-radius cell area as

$$P_{TC\ loss}^{Hbar} = \frac{\pi}{12} J_{sol}^2\, b^2\, R^2 \rho_{TC}. \quad (17)$$

Finally, in addition to the shadow cast by the major grid lines per (5), the bus casts a single shadow with power cost

$$P_{shadow\ loss}^{Hbar\ bus} = 2\ R\ J_{sol}\ V_{op}\ w. \quad (18)$$

These models include some nonphysical assumptions, most notably a total conservation of current, constant voltage across the solar cell, and negligible contact losses between TC and line. Nonetheless, we verify as described in Section II-C that the optimization of the numerical models yields near-optimum grid layout designs.

B. Grid Optimization

Numerical models were implemented as functions in Python for isotropic and H-bar grids. All numerical integration was carried out using the SciPy [32] integrate. quad() function, which invokes the Fortran QUADPACK library. Optimization of grid geometry means solving

$$\text{argmax}_{\{w,b\}}\ P_{max} - \sum_{l \in losses} P_l(w, b) + \lambda b^2 \quad (19)$$

where λ is a small constant that encourages larger grid pitch. This regularization is a practical term introduced because in the isotropic grid, the TC term $P_{TC\,loss} \propto b^2$ will drive an unbounded reduction in both w and b, pushing the grid to the lower design bounds consistently with minimal improvement in actual performance. Regularization of the grid geometry yields patterns that are less computationally strenuous for FE with minimal reduction in performance.

Optimal values of w and b are identified using SciPy's optimize. minimize() function, which employs the L-BFGS-B algorithm. For all grids, linewidth w had bounds [1 μm, $(R/2)$] and pitch b had bounds [1 mm, $(R/2)$], where R was the cell radius. The pitch lower bound was introduced to maintain practical computation burden in FE and was the only boundary condition to affect the grids generated in this study; the smallest designed linewidth in practice was 2 μm.

All codes used to model and optimize grids in this study can be found at https://github.com/onakanob/iso_grid_optimizer.

C. Grid Design Validation

The outputs of the numerical model and optimization loop were validated using Griddler, a free solar cell FE modeling package. We first verify the optimality of found grid patterns and the equivalence of the isotropic grid patterns. Then, we compare the performance of H-bar and isotropic grids across a range of solar cell and material properties.

A static operating voltage is manually chosen for the numerical model so that its optimal designs are also optimal in Griddler simulation. Fig. 3 shows that for a 1-kΩ/sq TC sheet resistance design, the two models are in close agreement on optimal pitch and width values when $V_{OP} = 420$ mV.

For all experiments, a set of standard centered conditions were specified for a circular 5-cm radius solar cell with a central current sink, 2-mΩ/sq metal grid lines, 0.5-mm sink radius, 420-mV operating voltage, and 20-mA/cm2 solar current. Griddler uses a double diode model for active material element simulation, and diode saturation currents of 450 fA/cm2 and 10 nA/cm2 were chosen. Griddler's internal optimizer was used to identify max-power operating voltage and current for each grid design.

Finally, the center condition TC sheet resistance value was chosen where isotropic and H-bar grids show equivalent performance. Fig. 4(a) shows that this occurs at about 15 Ω/sq. TC sheet resistance swept values range from 1 to 10^4 Ω/sq, covering from the low end of high-performance ITO layers to the upper range of TC materials considered by Jacobs *et al.* [19].

III. Results

For a solar cell at the center conditions described above, the model identified an optimal H-bar geometry of 7.8-mm pitch and 0.62-mm linewidth. Numerical power predictions are increased by a factor of 1.53 to bring center point predictions in line with the FE result. This factor is used to aid visualization as in Fig. 3, but it does not impact optimization results, which are unaffected by constant scaling. All performance values in Figs. 4 and 5 are unscaled outputs from Griddler simulations.

In Fig. 3, predicted power output from the numerical and FE methods are plotted around this optimal point, varying grid pitch and linewidth independently. The numerical model neglects the effects of voltage on current generation, causing some mismatch between the two models. However, with the tuned value $V_{OP} = 420$ mV, there is close agreement between the numerical and FE models on the optimal grid design. These trends illustrate the resilience of the grid design to perturbations—for instance, a 50% decrease in linewidth from the optimum results in just a 7% reduction in power density, from 6.9 to 6.4 mW/cm^2. Therefore, we do not expect small errors in grid design from our algorithm to be significant to the question of isotropic versus H-bar grids.

We compare the power output of circular solar cells with H-bar and isotropic front grid patterns given a range of cell geometries and material properties. Square grids were used to simulate all isotropic patterns. All simulations used solar cells at the centered conditions, but varying one parameter at a time. In Figs. 4 and 5, each of the cell's TC sheet resistance, grid line resistance, radius, and solar current density is varied systematically, and FE results for optimal grid power output of H-bar and isotropic grids are compared.

At center conditions, TC sheet resistivity is set at 15 Ω/sq so that both the H-bar pattern and the isotropic grid produce an equivalent 8.61 mW/(cm^2). While H-bars perform well at low sheet resistances below 15 Ω/sq, the isotropic grid

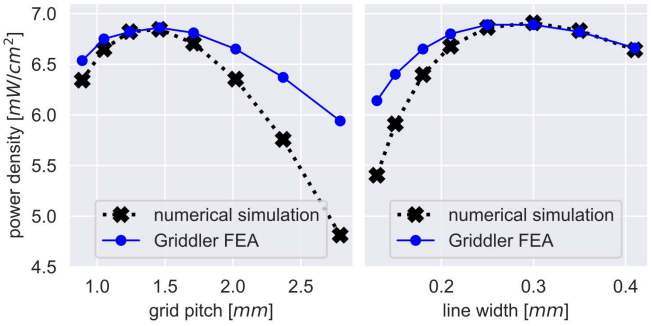

Fig. 3. Optimum values for grid pitch and linewidth found using numerical optimization are also near local optima in Griddler's solar cell FE when $V_{OP} = 420$ mV.

significantly outperforms optimal H-bar patterns for high TC sheet resistance values and shows more modest gains for large cell radii and elevated solar current.

IV. Discussion

While the H-bar grid continues to dominate performance with industry-standard TC sheet resistance values of <15 Ω/sq, isotropic grids matched or outperformed H-bars as front electrodes on center-sink circular solar cells with high TC sheet resistances and, to a lesser extent, large cell areas and high solar currents. The principal advantage of the H-bar design—its $2\times$ lower shadow loss coefficient—was present in these designs, but a combination of other factors gave the edge to isotropic patterns. These factors likely included a flat reduction in TC sheet losses, spreading transport burden across more metal elements, easier optimization landscape enabling fine-pitch patterns, and a reduction in voltage variance across the device stack.

TC resistive losses in both grids vary $\propto b^2$, with the isotropic grid experiencing lower loss by a constant factor of 8/3. The scaling factor implies that for any TC sheet resistance, a sufficiently small grid pitch will render resistive losses negligible. Conversely, sufficiently large pitch will cause TC losses to dominate device behavior. Contemporary solar cells usually deploy a front conductive transparent layer such as ITO with sheet resistance <10 Ω/sq, where millimeter-scale grid lines are sufficient to eliminate most TC losses and the isotropic grid's constant advantage has minimal utility. Under higher TC resistivity, reduction of the pitch value becomes critical to grid optimization. With very high TC resistivity, both grids in this study were clamped by the lower bound pitch of 1 mm, at which point the isotropic grid's flat 8/3 advantage becomes a significant performance driver.

The lower TC losses in isotropic grids arise due to the triangular unit cell across which current diffuses to grid lines, as shown in Fig. 4(c) and (d). This reduces the average distance from any point in the TC layer to the nearest grid wire from $(1/4)b$ for H-bars to $(1/6)b$ for square or hexagonal isotropic grids. More importantly, it reduces the average current density in the TC because current can spread with the triangle's cross section as it travels along the direction x toward a grid line, reducing resistive power loss.

An idealized solar cell might maintain a uniform max-power voltage across the entire device stack; in reality, a spread

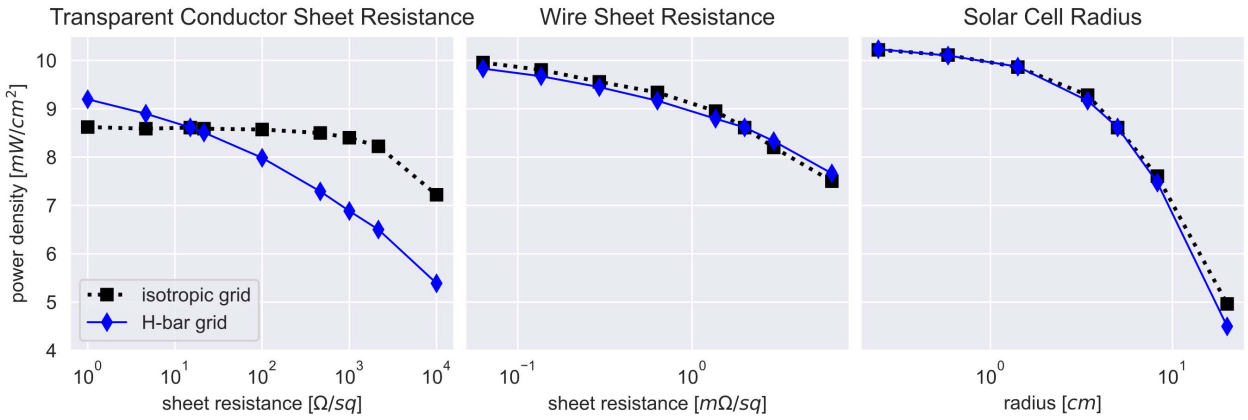

Fig. 4. Comparison of power density from H-bar and isotropic front grid solar cells with varying TC sheet resistance, wire sheet resistance, and solar cell radius.

of voltages around the max-power point arises across the solar cell due to resistance effects. The isotropic grid, by reducing resistance loss and thus voltage drops in the TC layer, is closer to the ideal case; this results in higher max-power voltage without losing too much photocurrent. To illustrate, at the lowest sheet resistance value studied ($R_{\text{sheet}} = 46$ Ω/sq), the optimal isotropic and H-bar grids both produced about 8 mW/cm^2. The two cells had a nearly identical open-circuit voltage of 622–624 mV, but the H-bar grid produced a much higher short circuit current, 18.6 mA/cm^2 versus the isotropic 16.6 mA/cm^2, due to its reduced shadowing. Despite the H-bar's current advantage, the max-power conditions for the isotropic grid of 523 mV and 15.58 mA/cm^2 matched the H-bar's 477 mV and 17.14 mA/cm^2 in terms of power output due to the isotropic grid's higher operating voltage, respectively. All effects of variable voltage and solar current are omitted from the numerical model, likely leaving some room for additional optimization in both grid designs.

The final weakness of the H-bar grid was its reliance on concentrated current flux through the single bus bar element—this introduces an additional constraint to its optimization problem and is largely a product of the assumptions in this study. In short, the H-bar grid wants larger linewidth to reduce bus bar loss but smaller pitch to reduce TC loss—this couples bus bar and TC losses, setting up a tradeoff in its optimization space that the isotropic grid does not need to deal with. The isotropic grid is, in fact, unconstrained in its specific choice of width and pitch except by TC loss considerations. $P^{\text{iso}}_{\text{grid loss}} \propto b/w$ and $P^{\text{iso}}_{\text{shadow loss}} \propto w/b$, so the isotropic grid optimizer only needs to find an optimal width-to-pitch ratio and can easily miniaturize the pattern to accommodate higher TC resistances, limited only by the simulation's lower bound and regularizing λ term.

This study assumed that current is generated in a circular area centered on the sink, a geometry chosen for its simplicity in assessing the relative performances of grid types. Such a module layout would seldom be encountered in industrial solar cell applications, where semisquare wafers or half cells and often multiple sinks per module are the norm. The extension of the model to any particular layout of sinks is

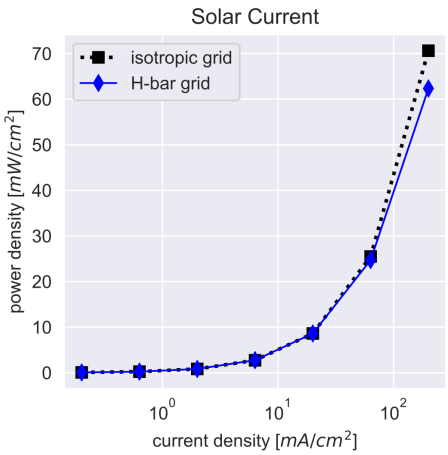

Fig. 5. Comparison of power density from H-bar and isotropic front grid solar cells with varying incident solar current.

left to the individual practitioner. However, the circular area assumption is likely to be a good approximation of any layout of sinks approaching a close packing. If isotropic grids are to find successful application in contemporary commercial solar modules, such as half-cut and the new C3 modules, a bus bar layout would need to be identified that leverages the area efficiency of close-packed point sinks while conforming to the overall rectilinear arrangement of those modules. The design of optimal bus bar layouts for isotropic grid solar cells is the next step to enable the comparison and competition of isotropic grids against real H-bar solar cell grid designs.

V. Conclusion

The foundational numerical models that established today's solar cell electrode designs deemphasized the utility of isotropic grids arrays of triangular, square, or hexagonal wire patterns—due to their higher degree of shadowing for equivalent conductive performance, compared to H-bar grids. However, in certain corners of the solar cell design space, isotropic grids are capable of outperforming H-bars. Isotropic grids have interesting properties, including an equivalence in shadow/resistance tradeoffs across all possible planar isotropic grid designs.

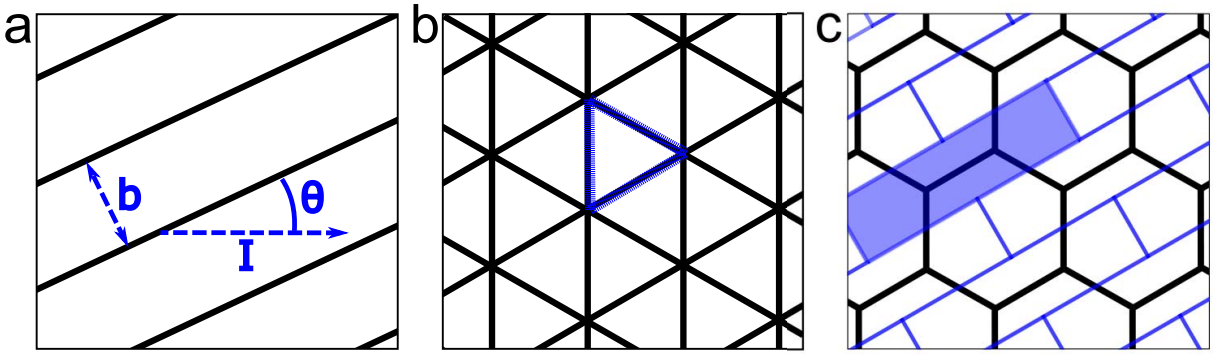

Fig. 6. Geometric conventions in describing the lack of angular dependence on grid conductivity: (a) grid angle, (b) overlay of three linear grids in a triangle isotropic grid pattern, and (c) unit tile for calculation of a linear subgrid in a hexagonal grid.

We have attempted to fill this gap in the modeling literature by presenting a simple numerical framework for modeling the shadow and resistive losses in circular, center-sink H-bar, and isotropic grids and for optimizing the pitch and width of the designs. Using Griddler FE software as validation, we demonstrate that isotropic grids produce more power for solar cells with high TC sheet resistance and point sinks. These designs could help enable a transition away from transparent conductive oxides and their associated processing, material, and optical costs, in favor of lightly doped electron or hole transport layers combined with fine front electrode grids. While the cutting edge of grid design has moved toward ramified networks and free-form design, the family of isotropic grids may still provide a performance baseline design, simple to optimize, and deploy, for the next generation of center-sink, ITO-free solar cells.

Appendix
Isotropy of Geometric Grid Patterns

To avoid confusion, a planar array of parallel conductive grid lines will be referred to as a "linear grid." Consider the "sheet conductivity" κ (in units squares/Ω or Ω^{-1}) of a linear grid with width w, height h, and material resistivity ρ_{metal}: $\kappa_{\text{sheet}} = (1/\rho_{\text{sheet}}) = (wh/\rho_{\text{metal}}\, b) = (1/\rho_{\text{wire}}\, b)$. Here, $\rho_{\text{wire}} = (\rho_{\text{metal}}/wh)$ is the resistivity of one line in the array, i.e. in units Ω/cm, and b is the grid pitch. These values apply only in the direction parallel to the lines in the array—indeed if current flux has no convergence, a design should simply align its grid with the current flux. With ϕ as the angle between the linear grid and the direction of current flux, effective grid line pitch and conductivity take on angular dependencies

$$\rho_{\phi,\,\text{wire}} = \frac{\rho_{\text{metal}}}{w\,h\,\cos\phi} \tag{20}$$

$$b_\phi = \frac{b}{\cos\phi}. \tag{21}$$

The angular sheet conductivity for the linear grid becomes

$$\kappa_\phi = \cos^2\phi\,\frac{wh}{\rho_{\text{metal}}\,b}. \tag{22}$$

Square and triangle grids are both comprised of multiple overlayed linear grids. Because all subgrids are continuous and in contact with each other, we model the complete system as several linear grids in parallel with offset angles $\Phi = \{\phi_1, \phi_2, \ldots\}$. The resulting conductivity is

$$K_{\text{grid}} = \sum_{\phi\in\Phi} \cos^2\phi\,\frac{wh}{\rho_{\text{metal}}\,b}. \tag{23}$$

If the involved grids have the same line properties and pitch, then the right-hand fraction carries out of the summation. With current traveling along direction θ, $\Phi_{\text{squares}} = \{\theta,\ \theta+\pi/2\}$ and $\Phi_{\text{triangles}} = \{\theta,\ \theta+\pi/3,\ \theta+2\pi/3\}$, and the summation reduces to a constant value—the lack of dependence on θ indicates that the grids have isotropic conductivity. In particular,

$$K_{\text{grid}}^{\text{square}} = \frac{wh}{\rho_{\text{metal}}\,b^{\text{square}}} \tag{24}$$

$$K_{\text{grid}}^{\text{triangle}} = \frac{3}{2}\,\frac{wh}{\rho_{\text{metal}}\,b^{\text{triangle}}} \tag{25}$$

and if the grids are sized so that $b^{\text{triangle}} = \frac{3}{2}b^{\text{square}}$, their conductivities will be equal.

The hexagonal grid solution is less clear because its component grid lines are not continuous. Instead, consider the unit tile shown in Fig. 6(c). The effective conductivity of the cell is 1/3 that of the metal line it contains because of the lengths relationship $l_{\text{wire}} = (1/3)l_{\text{tile}}$, and the tile cross section is $(1/2)$ of the grid pitch b. The sheet conductivity of a tiling of these partial-wire cells takes these scaling factors into account (such a tiling would not form a percolating electrical grid by itself)

$$K_\phi^{\text{hex}} = \cos^2\phi\,\frac{l_{\text{wire}}}{l_{\text{tile}}}\,\frac{wh}{\rho_{\text{metal}}}\,\frac{2}{b} = \frac{2}{3}\cos^2\phi\,\frac{wh}{\rho_{\text{metal}}\,b}. \tag{26}$$

As with the triangle grid, $\Phi_{\text{hex}} = \{\theta,\ \theta+\pi/3,\ \theta+2\pi/3\}$ and $\sum_{\phi\in\Phi_{\text{hex}}}\cos^2\phi = 3/2$. As a result, the hexagonal grid has an isotropic sheet conductivity equal to that of the square grid, so long as their pitches are equal

$$K_{\text{grid}}^{\text{hex}} = \frac{wh}{\rho_{\text{metal}}\,b^{\text{hex}}}. \tag{27}$$

This relationship holds only because current flux is constant in each of the overlapping hexagonal subgrids and the overall grid is fully connected (it percolates). Any such system with self-similar subgrids and Φ_{grid} comprised of more than two whole number divisions of the unit circle will also be isotropic—it follows that for any such isotropic grid, a pitch value exists, which renders it identical in conductivity to the isotropic grids discussed here.

Though we do not discuss it here in detail, it is apparent that a linear grid angle has no effect on its shadowing behavior and that the effect of line segment length and pitch scaling applies identically to shadowing. Furthermore, the multiplication trick used to find pitch values that bring conductivity in line between two different isotropic grids will also equilibrate the shadowing coverage of the two grids. Therefore, as far as we can tell, all isotropic grids will be fully equivalent to each other in their conductivity/shadowing tradeoffs, regardless of the particular number and angles of linear subgrids. We believe (but do not demonstrate) that this property extends in expectation to the properties of uniformly random arrays of conductive lines, such as nanowire assemblies.

REFERENCES

[1] L. S. Napoli, G. A. Swartz, S. G. Liu, N. Klein, D. Fairbanks, and D. Tamutus, "High level concentration of sunlight on silicon solar cells," *RCA Rev.*, vol. 38, pp. 76–108, Mar. 1977.

[2] H. B. Serreze, "Optimizing solar cell performance by simultaneous consideration of grid pattern design and interconnect configuration," in *Proc. Conf. Rec. IEEE Photovoltaic Spec. Conf.*, Jan. 1978, pp. 609–614.

[3] R. S. Scharlack, "The optimal design of solar cell grid lines," *Sol. Energy*, vol. 23, no. 3, pp. 199–201, 1979.

[4] M. Conti, "Optimal design of front-contact metallization for photovoltaic solar cells," *Solid-State Electron.*, vol. 24, no. 1, pp. 79–83, Jan. 1981.

[5] M. M. Shabana, M. B. Saleh, and M. M. Soliman, "Optimization of grid design for solar cells at different illumination levels," *Sol. Cells*, vol. 26, no. 3, pp. 177–187, Mar. 1989.

[6] F. Willing, S. Wiedeman, J. Newton, J. O'Dowd, and K. Jansen, "Power optimization for a-Si solar modules," in *Proc. IEEE Conf. Photovoltaic Spec.*, Kissimmee, FL, USA, May 1990, pp. 1432–1437.

[7] A. R. Burgers, "How to design optimal metallization patterns for solar cells," *Prog. Photovolt., Res. Appl.*, vol. 7, no. 6, pp. 457–461, Nov. 1999.

[8] A. R. Burgers, J. H. Bultman, A. C. Tip, and W. C. Sinke, "Metallisation patterns for interconnection through holes," *Sol. Energy Mater. Sol. Cells*, vol. 65, nos. 1–4, pp. 347–353, Jan. 2001.

[9] A. Cheknane, B. Benyoucef, J.-P. Charles, R. Zerdoum, and M. Trari, "Minimization of the effect of the collecting grid in a solar cell based silicon," *Sol. Energy Mater. Sol. Cells*, vol. 87, nos. 1–4, pp. 557–565, May 2005.

[10] L. Wen, L. Yueqiang, C. Jianjun, C. Yanling, W. Xiaodong, and Y. Fuhua, "Optimization of grid design for solar cells," *J. Semiconductors*, vol. 31, no. 1, Jan. 2010, Art. no. 014006.

[11] S. Braun, G. Micard, and G. Hahn, "Solar cell improvement by using a multi busbar design as front electrode," *Energy Proc.*, vol. 27, pp. 227–233, Jan. 2012.

[12] D. L. Meier, V. Chandrasekaran, A. Gupta, V. Yelundur, and A. Rohatgi, "Silver contact grid: Inferred contact resistivity and cost minimization in 19% silicon solar cells," *IEEE J. Photovolt.*, vol. 3, no. 1, pp. 199–205, Jan. 2013.

[13] F. Djeffal, T. Bendib, D. Arar, and Z. Dibi, "An optimized metal grid design to improve the solar cell performance under solar concentration using multiobjective computation," *Mater. Sci. Eng., B*, vol. 178, no. 9, pp. 574–579, May 2013.

[14] T. Panda *et al.*, "Impact of multi-busbar front grid patterns on the performance of industrial type C-Si solar cell," *Sol. Energy*, vol. 236, pp. 790–801, Apr. 2022.

[15] S. R. Wenham, M. A. Green, M. E. Watt, R. Corkish, and A. Sproul, *Applied Photovoltaics*, 3rd ed. London, U.K.: Earthscan, 2012.

[16] E. Van Kerschaver and G. Beaucarne, "Back-contact solar cells: A review," *Prog. Photovolt., Res. Appl.*, vol. 14, no. 2, pp. 107–123, Mar. 2006.

[17] J.-S. Yu *et al.*, "Silver front electrode grids for ITO-free all printed polymer solar cells with embedded and raised topographies, prepared by thermal imprint, flexographic and inkjet roll-to-roll processes," *Nanoscale*, vol. 4, no. 19, p. 6032, 2012.

[18] K. K. Sears, M. Fievez, M. Gao, H. C. Weerasinghe, C. D. Easton, and D. Vak, "ITO-free flexible perovskite solar cells based on roll-to-roll, slot-die coated silver nanowire electrodes," *Sol. RRL*, vol. 1, no. 8, Aug. 2017, Art. no. 1700059.

[19] D. A. Jacobs, K. R. Catchpole, F. J. Beck, and T. P. White, "A re-evaluation of transparent conductor requirements for thin-film solar cells," *J. Mater. Chem. A*, vol. 4, no. 12, pp. 4490–4496, 2016.

[20] C. Motta, F. El-Mellouhi, and S. Sanvito, "Charge carrier mobility in hybrid halide perovskites," *Sci. Rep.*, vol. 5, no. 1, p. 12746, Oct. 2015.

[21] T. Liu, W. Tang, S. Luong, and O. Fenwick, "High charge carrier mobility in solution processed one-dimensional lead halide perovskite single crystals and their application as photodetectors," *Nanoscale*, vol. 12, no. 17, pp. 9688–9695, 2020.

[22] D. Buzby, "Fine line screen printing of thick film pastes on silicon solar cells," *SGIA J.*, vol. 610, pp. 47–51, Nov. 2011.

[23] K.-H. Choi *et al.*, "Electrohydrodynamic inkjet—Micro pattern fabrication for printed electronics applications," in *Recent Advances in Nanofabrication Techniques and Applications*, B. Cui, Ed. Rijeka, Croatia: InTech, Dec. 2011.

[24] S. Lin *et al.*, "Roll-to-roll production of transparent silver-nanofiber-network electrodes for flexible electrochromic smart Windows," *Adv. Mater.*, vol. 29, no. 41, Nov. 2017, Art. no. 1703238.

[25] L. Kranz *et al.*, "High-efficiency polycrystalline thin film tandem solar cells," *J. Phys. Chem. Lett.*, vol. 6, no. 14, pp. 2676–2681, Jul. 2015.

[26] *Renewable Energy*, Monthly Energy Rev., U. E. I. Admin., Washington, DC, USA, Jun. 2021, pp. 175–194.

[27] C. D. Murray, "The physiological principle of minimum work II. Oxygen exchange in capillaries," *Physiology*, vol. 12, no, 5, pp. 299–304, 1926.

[28] C. D. Murray, "The physiological principle of minimum work: I. The vascular system and the cost of blood volume," *Physiology*, vol. 12, no. 3, pp. 207–214, Mar. 1926.

[29] D. K. Gupta, M. Langelaar, M. Barink, and F. van Keulen, "Topology optimization of front metallization patterns for solar cells," *Struct. Multidisciplinary Optim.*, vol. 51, no. 4, pp. 941–955, Apr. 2015.

[30] D. K. Gupta, M. Barink, and M. Langelaar, "CPV solar cell modeling and metallization optimization," *Sol. Energy*, vol. 159, pp. 868–881, Jan. 2018.

[31] J. Wong, "Griddler: Intelligent computer aided design of complex solar cell metallization patterns," in *Proc. IEEE 39th Photovoltaic Spec. Conf. (PVSC)*, Tampa, FL, USA, Jun. 2013, pp. 0933–0938.

[32] P. Virtanen *et al.*, "Scipy 1.0: Fundamental algorithms for scientific computing in Python," *Nature Methods*, vol. 17, pp. 261–272, Mar. 2020.